Available online at www.sciencedirect.com
SCIENCE DIRECT®
International Journal of Heat and Fluid Flow 25 (2004) 243–261
International Journal of HEAT AND FLUID FLOW
www.elsevier.com/locate/ijhff

Experimental investigation of local processes in pool boiling along the entire boiling curve

M. Buchholz [a], T. Lüttich [b], H. Auracher [a,*], W. Marquardt [b]

[a] Institut für Energietechnik, Technische Universität Berlin, Marchstr. 18, D-10587 Berlin, Germany
[b] Lehrstuhl für Prozesstechnik, RWTH Aachen, Turmstr. 43, D-52064 Aachen, Germany

Abstract

Understanding of fundamental local processes in boiling is a key to improved understanding of the boiling process in general and is therefore also a key for better insights using modeling and simulation studies. Unfortunately, only little experimental data is available with respect to local processes. Furthermore, data for boiling on technically thick heaters and for all boiling regimes is even more limited. Towards improved understanding of the boiling process, miniaturized sensors for measurements of the local boiling dynamics and spatial dimensions have been developed. For studies of the two-phase flow characteristics above the heater surface a 4-tip optical probe with tip diameters below 1.5 μm has been developed. Steady-state measurements along the entire boiling curve have been carried out for distances between heater and probe ranging from 20 mm down to positions as close as 8 μm. Microthermocouples have been developed for measurements of local temperature fluctuations inside the heater very close to the surface. Thirty-six of these thermocouples have been arranged on an 1×1 mm sized quadratic grid at the center of the heater. The junctions of the microthermocouples are located 3.6 μm below the heater surface. These thermocouples are very useful to study local temperature fluctuations and also spatial wetting dynamics. Selected measurements along the entire boiling curve are presented.

PACS: 07.07.Df; 07.20.Dt; 07.60.Vg; 42.81.Pa; 44.25.+f; 47.55.Dz; 47.55.Kf
Keywords: Microthermocouple; Optical probe; Pool boiling; Transition boiling; Dry patch; CHF; Boiling mechanism; Isopropanol; Two phase flow

1. Introduction

Knowledge and understanding of the boiling process is still not satisfactory. Despite a large number of investigations, many questions remain unanswered. New experiments are needed to clarify fundamental questions regarding the understanding of the processes, see Sadasivan et al. (1995). During the past decades, a large number of theoretical studies on modeling and simulation of boiling have also been published. These studies are focused on single bubble or bubble ensemble configurations as well as on models employing a more generalized approach for the prediction of nucleate boiling and/or CHF. As many of the authors point out, only little experimental data is available for the validation and further refinement of these models with respect to governing local mechanisms. This holds true especially for models addressing the high heat flux regions and the transition boiling region. Furthermore, experimental data is often limited to very few parameters so that additional assumptions are needed to validate the more sophisticated models. For a selection of studies focusing on dynamics and spatial dimensions of local phenomena, see Nishio et al. (1998), Kim et al. (2002) and Kenning et al. (2001).

This study aims at detailed experimental data on local temperature fluctuations at the heater surface as well as on vapor–liquid fluctuations above the heater for the entire boiling curve for a technically relevant thick (7 mm) heater. The study is an integral part of a research project on mechanisms in pool boiling with emphasis on the high heat flux regions of the boiling curve, see companion paper by Lüttich et al. (2003). By combining theoretical and experimental aspects in both the heater and the fluid region including also surface

* Corresponding author. Tel.: +49-30-314-25710; fax: 49-30-314-21-779.
E-mail address: auracher@iet.tu-berlin.de (H. Auracher).

0142-727X/$ - see front matter © 2003 Elsevier Inc. All rights reserved.
doi:10.1016/j.ijheatfluidflow.2003.11.020

Nomenclature

CHF	critical heat flux	PIF	phase indicator function
DPO	digital phosphor oscillograph	PSD	power spectrum density
fps	frames per second	$\dot{q}$	heat flux, W/cm^2
K_p, K_I	controller parameter	TC	thermocouple
LVDT	linear variable displacement transformer	w_m	mean velocity
MTC	microthermocouple	z	distance perpendicular to the heater surface
p^*	reduced pressure, p/p_c	α_v	void fraction

characteristics, boiling models with a degree of detail corresponding to the realizable experimental resolution can be developed. Employing this approach, unknown and hardly directly accessible variables such as the local heat flux fluctuations at the heater surface can be identified and then used as input for modeling and simulation of pool boiling. Hence, the use of assumptions on the subprocesses involved can be avoided.

For measurements of local boiling mechanisms for the concept described above, several requirements must be fulfilled: (a) sensors with sufficient fast response to resolve the dynamics of the local processes, (b) sensors with a sufficient degree of miniaturization to resolve the length scales of the local mechanisms and (c) a possibility for relatively long (30 s and above) measurements to allow adequate statistical analysis of the data. This requirement leads to the next two items: (d) controlled heater temperature for steady-state measurements along the entire boiling curve including the transition boiling region and (e) a data acquisition system capable of multichannel acquisition at high rate and resolution with sufficient duration for each test run. Simultaneous acquisition is strongly recommended, especially for measurements in the two-phase flow. As long as sensors with the necessary properties are not commonly available, the development of such sensors is a key to successful investigation of local boiling mechanisms. The first part (Section 2) of the paper describes the general experimental setup and the test heater. The second part (Section 3) presents the microthermocouples (MTCs) and optical probes developed for the studies as well as the control and data acquisition systems. The third part (Section 4) focuses on the experimental conditions and procedure as well as on data analysis. Results are presented in Section 5.

2. Pool boiling facility

2.1. Test loop

A scheme of the test loop is depicted in Fig. 1. The main components of the test facility are the boiling vessel (diameter 209 mm, height 332 mm), the vapor

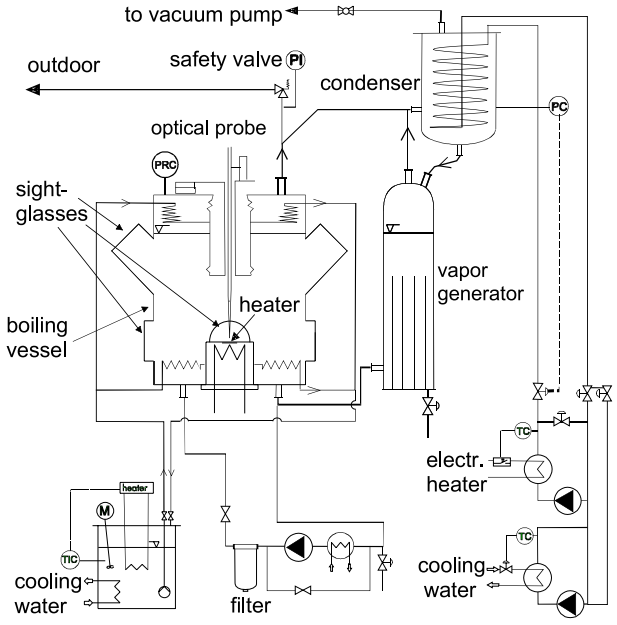

Fig. 1. Test loop and heater section.

generator and the condenser. The maximum operation pressure of the test loop for flammable test fluids is 0.7 MPa, otherwise 1.0 MPa. A filter loop with a heat exchanger, a hermetic centrifugal pump and a filter with an absolute removal rating of 0.2 μm can be used to remove small particles from the test fluid. Four sightglasses at heater level and two sightglasses at an angle of 45° allow observation of the boiling process. A recirculated temperature controlled bath filled with Thermogen 1693 (Clariant Company), a synthetic heat transfer fluid, is used to maintain constant saturation conditions in the test vessel via two tube coils. The vapor generator provides a basic load for the pressure controlled condenser. It also reheats potentially subcooled liquid from the condenser to preserve constant saturation state at the boiling vessel inlet. The condenser is cooled with a water/ethylene glycol mixture. Constant inlet conditions are realized by an electric heater and a heat exchanger, both temperature controlled. The coolant mass flow is controlled by a motorized control valve which is connected to a pressure control loop. The control loop is

described in Section 3.3. A probe can be installed at the top of the vessel. It can be moved in *XYZ*-direction with precision micrometer stages. The test loop is completely made from stainless steel, pickled, electropolished and passivated.

2.2. Test heater

A scheme of the test heater section is depicted in Fig. 2. The test heater is located at the bottom of the boiling vessel in a stainless steel housing. The boiling surface is horizontally positioned and has a diameter of 35 mm. The test heater is made from high purity copper and is 7 mm thick. It is cylindrical (5 mm high) in the top part and quadratic in the bottom part with 38 mm times 38 mm and 2 mm thick with the edges cut off. The boiling surface is coated with a pure gold layer of 1 μm thickness to prevent corrosion and oxidation of the surface. More details on this layer are given later in this section.

Heat input is provided by a resistance heating foil which is pressed on the bottom of the heater with a thin sheet of aluminium nitride ceramic in between for electrical insulation. The ceramic sheet is 0.25 mm thick, the heating foil is 25 μm thick. The maximum design heat flux is 5.5 MW/m^2 at the boiling surface.

Eighteen sheathed thermocouples with a diameter of 0.25 mm have been implanted in the test heater. Fourteen of these thermocouples are implanted 0.375 mm below the heater surface. They are used for measurement of the heater temperature, for heater temperature control (for a description of the control loop see Section 3.3) and for overtemperature protection. Four thermocouples are installed 1 mm above the bottom of the heater (6 mm below the heater surface). These thermocouples are also used for overtemperature protection. The thermocouples are installed in the heater as described in the next paragraph.

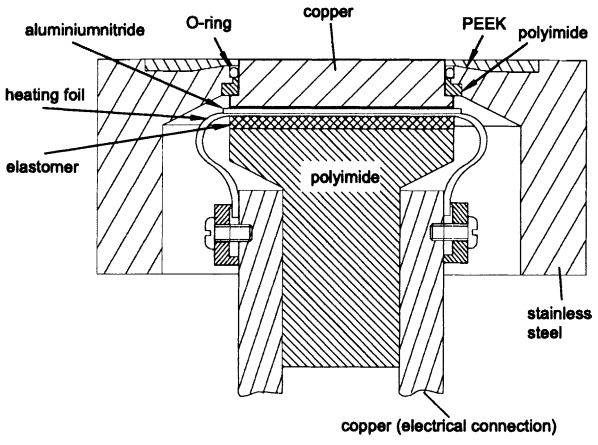

Fig. 2. Heater section.

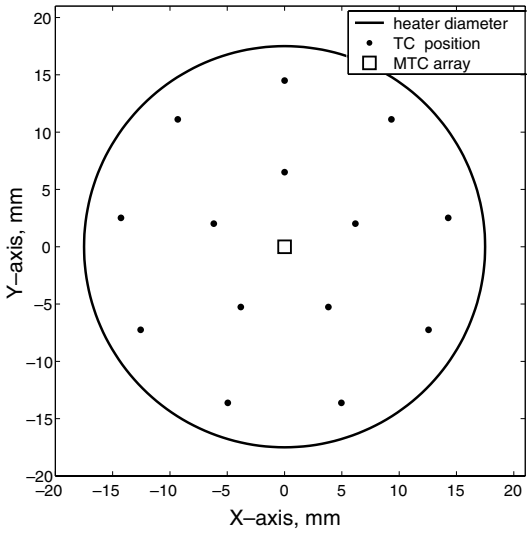

Fig. 3. Positions of sheathed thermocouples.

The heater preparation involves many different steps. First, a heater base is fabricated from high purity copper. Second, the contact area for the heating foil is prepared with grinding and then polished to mirror finish. The heater base is electroplated with a layer of nickel serving as diffusion protection and a gold layer. The latter protects the heater from corrosion during the following steps. Fourteen sheathed thermocouples are mounted on the surface afterwards. The positions of these thermocouples are depicted in Fig. 3. Then the microthermocouples (MTCs) can be installed. This process is described in Section 3.1. After installation of all sensors, the heater is coated with copper in an electroplating process. Excess material is cut off afterwards and the resulting surface is prepared with emery paper P 4000. At this stage, the MTC wires are visible at the surface and their true positions can be measured with a microscope measurement system. The final step of preparation is coating of the surface in a DC-magnetron sputtering process. Three layers are used: a 2.5 μm thick copper layer which serves as second conductor for the MTCs (see Section 3.1), then a 0.1 μm thick titanium layer to prevent diffusion between the copper layer and the top layer and finally a 1.0 μm thick pure gold layer. Because sputtering preserves the mechanical features of the surface, the boiling surface can be assumed to be prepared with emery paper P 4000 although it has never been in contact with emery paper at all.

The roughness structure of the boiling surface is measured afterwards with a 3-D scanning ultrasonic stylus instrument (for more details see Luke (2003)). The surface topography of the boiling surface is depicted in Fig. 4. The measured area is directly above the center of the heater under which the microthermocouple array is installed, see Section 3.1. The roughness measured with the same contactless measuring method as

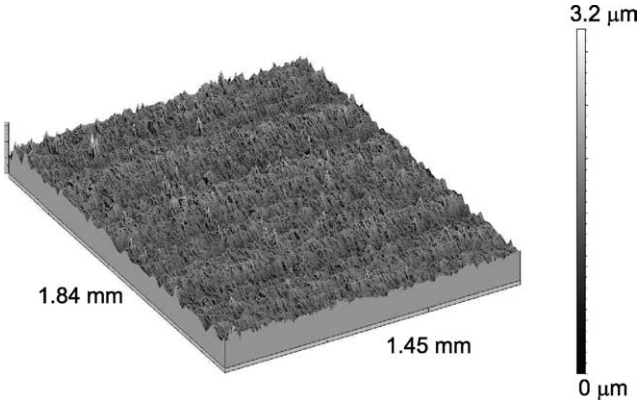

Fig. 4. Topography of heater surface above MTC field.

described above is $P_{a,\mathrm{mean}} = 0.113$ μm and $P_{Z,\mathrm{mean}} = 0.549$ μm. The analyzed length is 0.5 mm with a filter cutoff of $\lambda = \infty$.

3. Miniaturized sensors, data acquisition and control

3.1. Microthermocouples (MTCs)

Since even the smallest standard sheathed thermocouples cannot resolve the temperature fluctuations at the heater surface with sufficient accuracy with respect to spatial and temporal dimension, smaller and faster sensors are necessary. Thus, special microthermocouples have been developed for these experiments. The schematic setup of the microthermocouples is depicted in Fig. 5, the dimensions of the grid in Fig. 6. Each thermocouple consists of an insulated Constantan thermocouple wire which is embedded in the heater. The second conductor of the thermocouple is a sputtered copper layer on top of the heater preform (see Fig. 5 and Section 2.2) which is contacted with insulated Copper thermocouple wires. The resulting thermocouple of type "*T*" has a circular shape of the sensitive area which is only little larger than the wire diameter itself. Although smaller wires are possible and have also been used, the Constantan wire diameters used here are 38 μm and 50 μm, the diameter of the Copper wires are 50 μm. The distance between the junction and the heater surface is given by the total thickness of the sputtered material (3.6 μm) on top of the heater. According to the characteristics of the sputtering process and deposition rate calibration of the industrial-size facility, the thicknesses are known with high precision and thickness variations across the surface are negligible. This results in identical response characteristics for all thermocouples with the same wire diameter.

The preparation of the thermocouples is carried out as follows. First, the Constantan thermocouple wires (38 or 50 μm conductor thickness, Polyimide insulation, 6.7

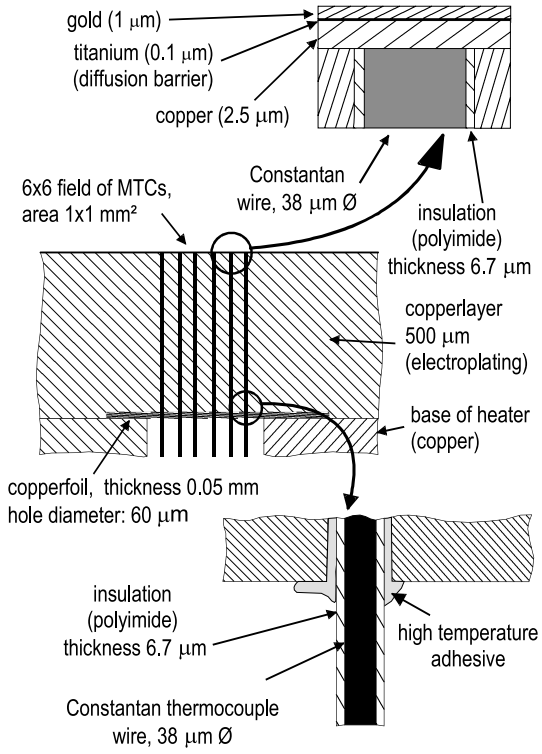

Fig. 5. Setup of microthermocouples.

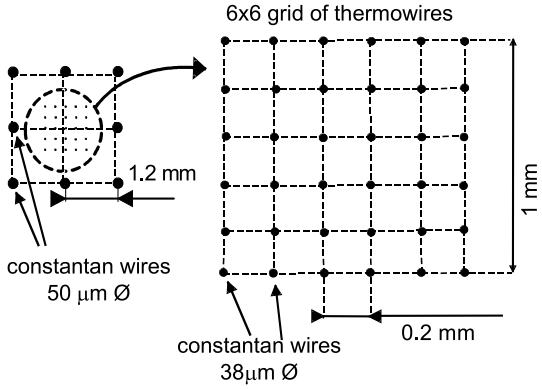

Fig. 6. Designed positions of microthermocouples.

and 5.7 μm thick, respectively) are labeled for identification purposes. A thin copper foil is prepared with holes of approx. 60 μm diameter, arranged in a rectangular grid of six rows with six holes each row, giving 36 holes in total. The spacing between the rows is 200 μm so the total space spanned by the hole centers is 1 mm^2. The 38 μm Constantan wires are placed through these holes and then fixed with a high temperature adhesive. The foil with fitted Constantan wires is placed on the base of the heater and fixed with a high temperature adhesive (Epo-Tek 353 ND, Polytec Company). The Constantan wires run through a small hole to the side of the heater for electrical connection to the thermocouple amplifiers. At this point of preparation, 8 additional

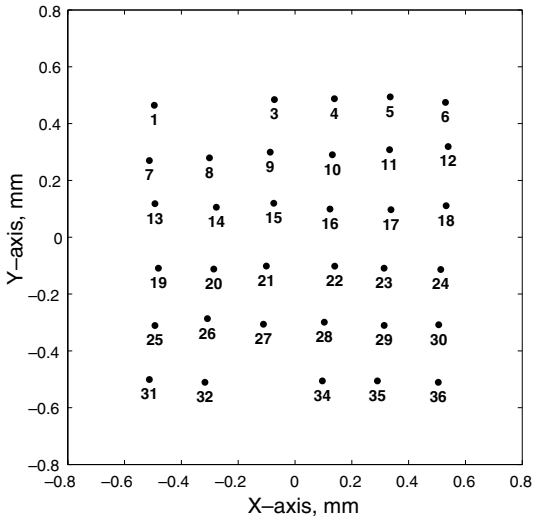

Fig. 7. Measured positions of 1×1 mm MTC array.

Constantan thermocouple wires with 50 μm diameter are mounted around the center grid manually under a microscope. The same procedure follows for 8 Copper wires which contact the copper layer after the final steps of preparation as described in Section 2.2. Prior to the sputtering of the top layers, the real *XY*-positions of all MTCs are measured using a calibrated microscope measurement system. The real positions of the used MTCs and their numbers can be seen in Fig. 7. MTCs nos. 2 and 33 are omitted because these elements are not working, the ring of MTCs is not plotted to improve visualization of the center field. The result of the described installation process is a six times six sensors array of fast response thermocouples on an area of 1 mm^2 and an additional ring of 8 fast response thermocouples around this grid.

This method of preparation enables installation of miniature thermocouples very close to the heater surface without a local effect on surface characteristics like surface roughness or surface wettability, because the entire surface of the heater preform is prepared in an identical manner and afterwards uniformly coated by sputtering. Sputtering preserves the mechanical features of the surface roughness as can be seen in the 3-D topography measured above the microthermocouple grid (see Fig. 4). As can be seen, the thermocouple wires below the surface do not influence the surface characteristics. The same holds for chemical surface properties because the surface is evenly coated with the same material. However, one effect cannot be excluded: the local change of the thermal conductivity due to different materials (thermocouple, insulation, copper) could have an effect on the boiling process. The local temperature distortion as a measure for this effect was minimized during the design process using a simulation study of different designs of the MTC-array with various spacing of the MTCs and various thicknesses of the sputtered layers.

3.2. Two-phase flow/optical probes

Two phase flows associated with boiling exhibit a wide range of parameters such as void fraction, contact frequency and bubble diameter. For example, the local void fraction can be close to *zero* at the onset of boiling and *one* in film boiling at a position very close the the heater surface (see Hohl et al., 1998). Furthermore, the dynamic properties of the local flow are not well known. All these characteristics prohibit the use of non-intrusive methods such as high speed video, X-ray scanning or thermal neutrons as they cannot access the local parameters in the degree of detail needed here.

Miniaturized optical probes provide access to these parameters. They are well known for local measurements of liquid–vapor two phase flows. They are also known for the high accuracy of the measurements (see Arosio et al., 1999). In the past, most optical probes have been used in two phase flows with relatively large bubble diameters and large axial distances between the probe and a wall. In this type of flow, the disturbance caused by the probe with a standard tip diameter is not critical. The tip diameters of probes published in the literature are typically in the range between 10 and 150 μm. In pool boiling, however, the situation is different. First, measurements with very small distances to the heater surface should be possible without significant disturbance of the flow because the important process of interfacial area generation takes place at the heated wall. Thus, measurements should be realized very close to the heater surface. Second, bubble sizes in boiling of common boiling fluids—refrigerants for example—are much smaller than in air–water or steam–water flow at atmospheric pressure. Therefore an optimized optical probe has been developed.

The optical probe system is based on an earlier development by Hohl et al. (1998). A light source sends infrared radiation via a beam splitter into the optical fiber. Depending on the refractive index of the fluid at the probe tip, the light leaves the probe tip (liquid) or is reflected back into the fiber (vapor). An optical receiver at the end of the fiber provides an electrical signal. The optimized optical probe is made from single mode quartz glass fiber with a cladding diameter of 125 μm and a core diameter of 8 μm (see Fig. 8). A laser diode with a wavelength of 1300 nm serves as light source. The laser light used to operate the probe travels along the core only. The tip of the probe is formed by etching in hydrofluoric acid. This method enables the preparation of very small probe tips. Measurements of the probe tip dimensions with a scanning electron microscope give a tip diameter of less than 1.5 μm (see Buchholz and Auracher (2002) for more details).

The probe is operated by an electronic detection unit. The main part is a bidirectional optical unit Bidi®

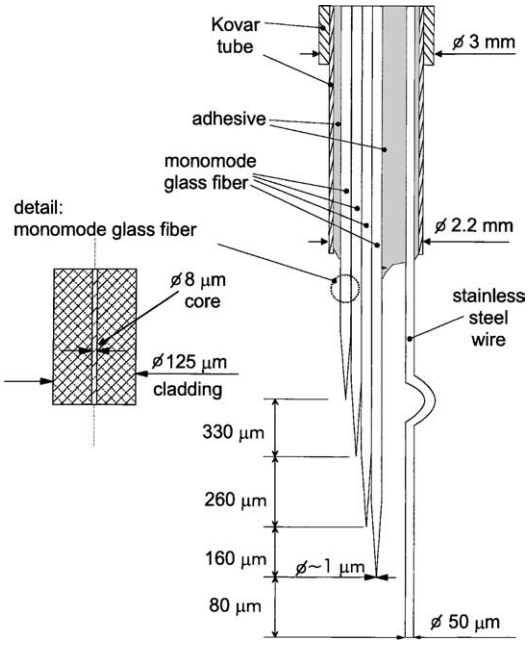

Fig. 8. Setup of 4-tip optical probe.

(Infineon AG) which contains all necessary parts: a laser diode, a beam splitter and a PIN-photodiode in a single device. The detection unit contains also electronics for safe operation of the laser diode and amplification of the detected signal. More details of the probe setup can be found in Buchholz and Auracher (2002).

The position of the probe can be set in X–Y–Z direction with micrometer stages equipped with micrometer screws. The position perpendicular to the test heater—the Z-axis—is measured both with the precision stage and at the same time with a precision LVDT-displacement sensor. The accuracy of the sensor is ±1.1 μm.

The optical probe system has been validated for the case of a twin optical probe with an axial probe distance of 425 μm with a droplet impingement experiment. These tests prove low measurement error less than ±5%. This measurement error is mainly given by the optical and temporal resolution of the test setup itself. For the validation experiment, a high speed video camera (Speedcam Pro, Weinberger AG) at 2000 fps and a high speed synchronized flash illumination (Speedflash, Weinberger AG) was used. The real measurement error is most likely well better than this conservative estimate from the validation experiments. The tests also show that the probe has an influence on the shape of the droplet interface. Fortunately, this deformation does not affect the accuracy of interface detection because the detection takes place *prior* to a visible deformation. This fact is most likely a result of the very small tip diameter—the small tip detects the interface and *then* the interface is being deformed at the larger fiber diameter above the tip. More details of the probe validation can be found in Buchholz and Auracher (2002).

Four of these optical probes have been combined to form a 4-tip optical probe (see Fig. 8). The optical fibers are placed next to each other with different axial distances. A stainless steel wire with 50 μm diameter for distance calibration is installed with about 800 μm radial distance to the lower probe. The wire allows the calibration of the probe position by detecting an electrical contact between the wire and the heater surface. All positions, including the detection wires, have been set to the desired positions with precision micrometer stages and controlled with a calibrated microscope measurement system. The realized distances are listed in Table 1. Although the distance between the lowest probe and the detection wire is 80 μm, the minimum probe distance is not limited to this value (see Table 2). Measurements very close to the heater surface are possible because the stainless steel wire has been coiled to form a 1-winding spring (see Fig. 9). This spring allows the probe to be

Table 1
Distances between optical probes

Axial distance to lowest probe (μm)	Distance between probes (μm)	Item
−80		Detection wire
0		First (lower) probe
	$\Delta z = 160$	Probe 1–2
160		Second probe
	$\Delta z = 260$	Probe 2–3
420		Third probe
	$\Delta z = 330$	Probe 3–4
750		Forth (upper) probe

Table 2
Measured optical probe positions above the heater

Distance between heater surface and lowest probe				
8 μm	100 μm	850 μm	3.3 mm	15 mm
30 μm	350 μm	1.35 mm	4.5 mm	20 mm
50 μm	450 μm	2.3 mm	10 mm	

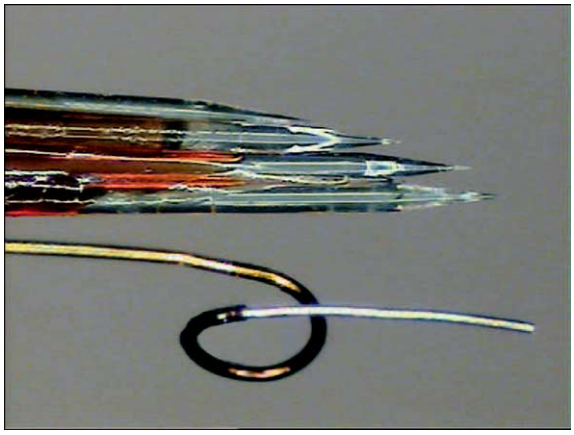

Fig. 9. Photograph of 4-tip optical probe.

moved very close to the surface without a permanent change of the detection wire position or an effect on the optical probes.

The radial distance between any two probes which are next to each other in axial direction, is given by the fiber diameter and therefore 125 μm. The distance to the detection wire was chosen to be greater to minimize possible effects of the wire on the measured two-phase flow structure. The radial distance is approx. 800 μm.

All optical fibers and the stainless steel wire are glued together with a high temperature adhesive. The probe array is sealed with the same high temperature adhesive into Kovar tubes (low coefficient of thermal expansion) of different diameter to achieve minimum flow disturbance and sufficient stiffness of the probe. The Kovar tubes are gold plated from the outside to maintain test fluid purity. A microscope picture of the 4-tip optical probe is depicted in Fig. 9.

3.3. Control system

3.3.1. Heater temperature control

Various control loops maintain constant operation conditions during the experiments. First, a heater temperature controller allows steady-state measurements along the entire boiling curve. This controller is realized as a discrete controller on a PC. The controller runs independent of the PC processor on a signal processor card with onboard DSP processor (AT-DSP2200, National Instruments). For the temperature control loop, the instantaneous average of 12 temperatures below the heater surface is used as temperature input. These temperatures represent the average heater temperature. The total response time between a temperature change at the input and the response of the controller at the output is less than 1.5 ms. The output is amplified and supplied to the heating foil. Maximum heating current is 350 A, the maximum heat input about 5.5 kW.

3.3.2. Pressure control

The pressure in the boiling vessel is controlled to maintain constant pressure even with large changes of the heat flux at the test heater. This controller is realized on a PC (PIII, 733 MHz) with the software Lab View (National Instruments) and installed multifunction data acquisition cards (see Section 3.4). The output of the controller sets the position of a motorized coolant control valve (see Fig. 1).

3.3.3. Guard heaters

Two independent guard heaters maintain constant temperature of the copper connectors of the heating foil to minimize heat losses of the test heater (see Fig. 2). These control loops are also implemented in LabView as described above. Two high power operation amplifiers (DCP 520, Servowatt Company) amplify the output voltage of the multifunction cards to drive heating resistors on the copper connectors.

3.4. Data acquisition

The data acquisition system is adapted to the different characteristics of the signals. Measurements of standard signals run always parallel to the acquisition of MTC- or optical probe signals.

Standard signals like pressure, temperature, heating voltage and current etc. are acquired with a PC (PIII, 733 MHz) with two installed data acquisition cards (16 Bit, DaqBoard 2000, IOtech) and one expansion card. Sampling rate is 100 Hz per channel. Voltages of standard thermocouples are amplified prior to acquisition by factor 700 and filtered with a 4th order lowpass with 1 kHz cutoff frequency. Other ''standard'' signals are conditioned to fit in a standard 0–10 V input range.

Signals from sensors which require fast acquisition as optical probes or microthermocouples are acquired with two ADC-64 cards for PC. Each card has 8 A/D converter (each converter 16 Bit, 200 kHz max. sampling rate), 32 differential inputs and an onboard DSP-processor (Innovative Integration). Each card enables simultaneous sampling on groups of 8 channels which is important especially for optical probe measurements. A special burst mode software allows minimum time lag between the channel groups 1–8 to 25–32. This mode is used for the microthermocouple measurements. The result is an almost simultaneous acquisition of the microthermocouple signals. Because of the large data streams, only one card can be installed in one PC. For this purpose two additional PCs (PII 400 MHz, SCSI 2 UW, 256 MB RAM and an Athlon 1 GHz, 384 MB RAM) are used. Both cards are synchronized with the main data acquisition PC by digital signals. The lowpass filters on board the ADC-64 cards are disabled.

3.4.1. Setup for MTC measurements

For the experiments with microthermocouples, both PCs with ADC-64 cards are used. The sampling rate per input channel is 25 kHz. All microthermocouple voltages are amplified by factor 700 and low-pass filtered with a 4th order lowpass with 7.5 kHz cutoff frequency prior to acquisition.

3.4.2. Setup for optical probe measurements

For measurements with optical probes, one ADC-64 card is used with 200 kHz sampling rate per channel. The duration of all test runs was 60 s. This duration is selected because of two reasons. First, the file size of up to one-minute runs at 200 kHz (about 800 MB ASCII-data for 60 s) permits later analysis without large numerical difficulties. Second, limited disk storage space would imply a reduced number of measured positions and/or temperatures along the boiling curve using longer

test durations. All probe signals are additionally monitored during the experiments using a 4-channel DPO oscillograph TDS 3014B (Tektronix). The scope readings provide the necessary information for the selection of heater temperature (online void fraction estimation) and to assure safe probe operation (see Section 3.5).

3.5. Calibration of optical probe position

The distance between the 4-tip optical probe and the heater surface is calibrated using the stainless steel wire next to the probe (see Section 3.2 and Fig. 9). The calibration is carried out under low heat flux boiling condition. For the distance calibration, the probe is moved towards the surface very slowly. At the first electrical contact between wire and the heater the distance is 80 μm, because the wire has been set to this position during probe preparation. The reading of both the micrometer screw and the LVDT distance sensor are saved. For the experiments, all distances up to 1.5 mm distance are set using the LVDT reading, larger distances with the micrometer screw reading. At the lowest measured distance (8 μm), an additional distance control was made. This is possible, because the probe signal increases if the probe is located closer to the heater than 8 μm. This effect is caused by a reflection of the emitted infrared laser light at the heater surface. At least a part of the reflected light is detected by the probe electronics. For the distance check during an experiment, the probe located at 8 μm is moved very slowly towards the surface with simultaneous measurement of the low signal level with a DPO oscillograph. At about 6 μm probe distance, a level increase was detected. This test was performed for boiling setpoints between nucleate boiling and film boiling with identical results. The total distance error is therefore expected to be less than ±2 μm for distances up to 1.5 mm and less than ±10 μm for larger distances.

4. Experimental procedure, data evaluation

4.1. Experimental conditions and procedure

All experiments are performed with saturated isopropanol at a reduced pressure of $p^* = 0.022$ which represents a pressure of 0.104 MPa and corresponds to a saturation temperature of 82.9 °C. For optimum test fluid purity the entire fluid is charged in vapor state and condensed in the facility. The test liquid is thoroughly degassed previous to the experiments by vigorous boiling of the test liquid and repeated removal of inert gases at the top of the condenser. All experiments are carried out in steady-state. After the facility has reached steady-state (for ex. temperatures of boiling vessel and probe support as well as operation pressure) and saturated fluid conditions are reached, experiments can be started. To prepare for a test run, the heater temperature controller is set to a temperature for high heat flux transition boiling to activate possible nucleation sites in order to avoid hysteresis at boiling incipience. The heater temperature is afterwards set to the first point of a test run and the measurements are started after steady state of the test heater is reached. Then the temperature is set to the next value until heat transfer at all desired heater temperatures have been measured.

Two test series are presented in this paper: (1) measurements with MTCs along the entire boiling curve (Section 5.1) and (2) measurements with optical probes at various probe positions and some boiling setpoints (Section 5.2). For the optical probe test runs, all probe positions are measured one after each other at constant heater temperature. After the last probe position, the temperature setpoint is changed to the next value and again all probe positions are measured. The measurements are realized with stepwise increasing temperature between low superheat and high superheat. The selected positions of the 4-tip optical probe are listed in Table 2. The 4-tip optical probe is located above the center of the heater.

4.2. Evaluation of the boiling curve

The duration of the measurement for each point of the boiling curve is 60 s, depending on the chosen duration of measurement for the sensors. All used measurement durations are well above the needed duration for good reproducibility. After conversion to physical units the data for each point of a boiling curve is averaged except for heating voltage and current. The latter are pointwise multiplied and then averaged to the calculate heating power. The resulting boiling curve is depicted in Fig. 10.

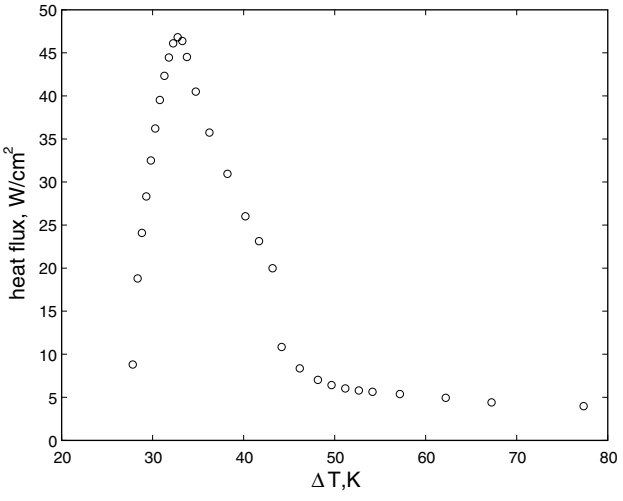

Fig. 10. Boiling curve.

4.3. Evaluation of MTC signals

For the analysis of the MTC data a good signal to noise ratio is important. Although the setup of the measurement chain for MTC signals is optimized for best signal integrity, some noise can be found in the signal. Unlike standard temperature measurements, averaging or simple filtering techniques can not be applied as they would destroy the signal dynamics (see also Fig. 13). To design the data preparation scheme, the signal characteristics are analyzed from measurements with a discharged boiling facility and therefore without boiling components in the signal. The typical raw signal has a base noise level of about ±0.05 K and additional relatively rare spikes of up to ±0.15 K.

The analysis uncovers three main types of noise. Noise type *A* is random noise generated by the MTCs itself and by cables and the thermocouple amplifiers, to a minor part also by the data acquisition (very high frequency components). Noise type *B* is pickup of line noise and multiples, i.e. 50, 100, 150 Hz and above. Type *C* noise are signal spikes caused by electrical interference between the data acquisition systems and line voltage transients. This type of noise has by far the largest signal amplitude of all noise types, but because of the very short and rare spikes the influence is weak.

Because of this fact, noise type *C* is not removed in order to preserve best signal integrity. Noise type *B* can be removed using digital stop band filters. Digital zero phase lag (forward–backward) filters are used to perform this task as they maintain correct signal timing. The filters are designed with narrow bandwidth for minimum effect on the signal, just to give a smooth PSD without peaks remaining at the filtered frequencies. Noise type *A* has an acceptable low amplitude. Therefore only a 6th order digital lowpass (also zero phase lag) with a cutoff frequency of 8 kHz is used to remove the high frequency components caused by the data acquisition itself. The MTC signal does not contain meaningful high frequency components above the cutoff frequency because a hardware lowpass filter with 7.5 kHz cutoff frequency is used during acquisition to avoid aliasing (see Section 3.4).

The data preparation is performed in the following order: line noise filtering, low pass filtering and finally conversion to temperatures.

4.3.1. Temperature field visualization

To visualize the temperature field of the heater the prepared temperature data (see Section 4.3) at each MTC is used. Therefore the data represents the temperature field 3.6 μm below the heater surface. The data of all MTC at their known positions (see Section 3.1) for each point of time are used to generate a matrix which contains the *XY*-locations and the corresponding temperature for the pixels at the MTC positions. Temperatures for the pixels in between the MTC positions are interpolated between neighboring MTCs. This matrix is then visualized, using the temperature to set the color of each pixel. For information on the MTC locations, see Fig. 7. Subsequent temperature field images are then combined for a movie which is used to visualize the dynamics of the boiling process.

4.4. Evaluation of probe signals

The signals of the optical probes basically contain a binary information: vapor or liquid phase at a given moment at the probe tip. This information can be represented with a Phase Indicator Function PIF:

$$\mathrm{PIF}(\vec{x},t)=\begin{cases}1 & \text{for vapor}\\ 0 & \text{for liquid}\end{cases} \tag{1}$$

To extract this binary information from the raw signal an analysis procedure is used. The PIF identification method is based on an algorithm developed by Hohl (1999). It is optimized and adapted to the characteristics of the new optical probes.

The calculated PIFs are the data basis for all analysis of the two phase flow characteristics. The first step of the analysis towards the PIF is filtering of the raw signal to remove noise which is basically optical noise, most likely from the laser diode, its drive cirquits and the optical fiber itself. The denoising process is based on wavelets as this approach allows removal of noise at low and high signal levels while preserving the characteristic steep changes of the signal at fluid phase changes at the probe tip which are essential for precise detection of the phase changes. Although detection of the PIF without denoising of the raw probe signals is possible, denoising improves confidence of the following PIF detection process and allows usage of a faster detection algorithm than without denoising. The next step towards the PIF is calculation of the average signal levels representing liquid and vapor phase. These levels are used to limit the low signal level to the average liquid level and vice versa for the high signal level (vapor). The limiting of the signal to the average bounds avoids misinterpretation of signal overshoot at liquid to vapor transitions (for more information on overshoot, see Buchholz and Auracher (2002)). For the decision if the signal at a point i represents vapor or liquid, the detection algorithm calculates the differences between i and $i-1, i+1, \ldots, i+N$ with $N \leqslant 4$. A phase change at point i is identified, if there is a sufficient change between $i-1$ and i or, if there is a smaller change between these points but the criteria is fulfilled for any of the calculated differences. An additional check for the signal level follows to permit also detection of very slow signal changes. Slow signal changes are very rare, but the check improves the confidence of the calculated PIF. The algorithm can be classified as a combination of an optimized

differentiation method and the two-level method. The PIF analysis is realized as follows. Each sensor signal is read from disk, then evenly divided into 10 s long (2 million data points) sections which are filtered and fitted together again to filter the total signal length. Level detection, limiting and finally the PIF detection process follows. The sectional approach for the filtering is necessary because even 1.5 GB RAM do not permit filtering of the entire 60 s long data section. The calculated PIFs are compressed and stored on disk for later analysis. The PIF detection process alone consumed about 70 h computation time on a 1 GHz Athlon PC for the data presented in this paper.

The average void fraction at a given probe location z can be calculated from the PIF as

$$\alpha_v(z) = \frac{1}{N}\sum_{i=1}^{N} \mathrm{PIF}(i,z) \tag{2}$$

All average void fraction data points are calculated using the entire 60 s long data set (12 million data points).

As a first approach towards a mean interface velocity perpendicular to the heater surface, the cross-correlation function can be used. For this purpose, only the time lag at the maximum of the cross-correlation is of interest. Therefore, calculation of the entire function is not necessary. Numerical restrictions (large signal size) and desired accuracy force to use a direct calculation of the cross-correlation for the region of interest. After calculation of the cross correlation coefficient, the time at the peak maximum can be identified. The mean velocity of the interfaces can then be calculated as

$$w_{m,i}(Z) = \frac{\Delta s_i}{\Delta t_i(z)} \tag{3}$$

with Δs_i, the axial distance between the correlated probe pair $i = 1,\ldots,3$ and $\Delta t_i(z)$ the identified time lag at probe position z of the maximum of the cross-correlation coefficient. The cross correlation coefficient is presented as "a first approach" towards a mean interface velocity, because we believe that there are better options to calculate the velocity than using the cross correlation coefficient. The main reason is that the cross correlation coefficient analyzes the entire signal no matter what the underlying physics are. An adopted algorithm will be presented in the future.

5. Results

The steady-state boiling curve is depicted in Fig. 10 for reference purposes.

5.1. Microthermocouple experiments

Typical traces of the measured temperature at the microthermocouples nos. 3 and 4 are depicted in Figs. 11 and 12. The horizontal distance between their thermocouple junctions is 211 μm.

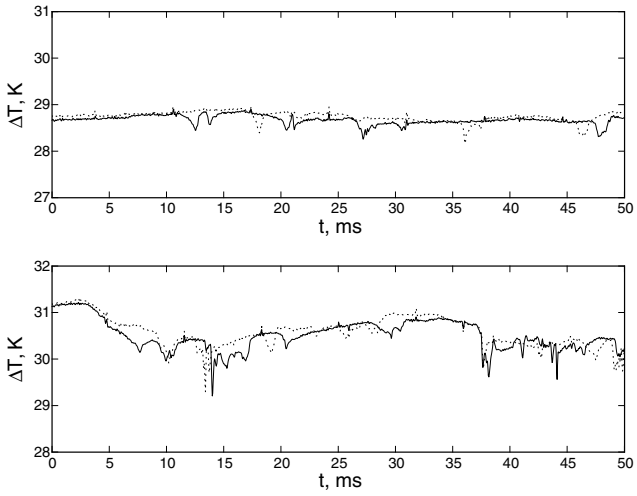

Fig. 11. Temperatures at MTCs nos. 3 and 4; top: nucleate boiling ($\dot{q} = 29$ W/cm^2), bottom: CHF.

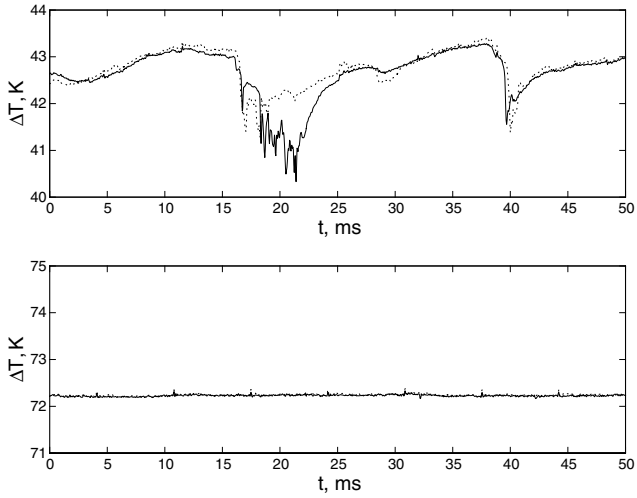

Fig. 12. Temperatures at MTCs nos. 3 and 4; top: transition boiling ($\dot{q} = 11$ W/cm^2), bottom: film boiling ($\dot{q} = 4$ W/cm^2).

Although a complete representation of the signal dynamics is not possible with only few plots, the temperature traces in Figs. 11 and 12 give a good impression of the typical signal dynamics. As can be expected, the amplitude of the temperature fluctuations increases with increasing wall superheat. This is because the temperature should only drop to at most saturation temperature. Thus, the theoretically possible fluctuation amplitude increases with increasing superheat. In film boiling no temperature drops can be found in the signal which means that surface wetting does not take place. Sharp temperature drops can be found in nucleate boiling, CHF and transition boiling. These events point most likely to ongoing nucleation and growth of a

bubble above the MTC junction in nucleate boiling. In transition boiling, a temperature drop can be interpreted as a surface rewetting and subsequent nucleation and growth of small bubbles because there are unstable vapor patches present intermittently at the surface. In low heat flux (high superheat) transition boiling no liquid rich layer is present at the heater surface (see following Section 5.2 on optical probe measurements). In transition boiling, the temperature transient during a rewetting period can exceed −10 000 K/s.

Looking at the signals more closely, some interesting features can be found. On the one hand, rapid temperature drops and the associated bubble nucleation events seem to be very local events because even at the neighboring MTCs (distance 211 μm) some fluctuations occur independently at both MTC junctions. These sharp temperature drops are not well correlated. On the other hand, slow temperature changes—compared to the very rapid changes during nucleation or rewetting—are much better correlated at neighboring MTCs, see Fig. 12 (top) and also Fig. 11 (bottom). This points most likely to the existence of larger structures on the surface like dry patches in transition boiling. Within these dry patches the measured temperature at neighboring MTCs can be expected to be similar because of thermal conduction within the heater. The same holds for areas without bubble nucleation in low heat flux nucleate boiling.

These results are in general agreement with results published in the open literature. Moore and Mesler (1961) were probably the first to develop a surface thermocouple. They used a nickel layer on top of their TC with about 1.3 μm thickness. They reported fluctuation amplitudes between 11 and 17 K in nucleate boiling of water. Nishikawa et al. (1972) used two different miniature thermocouples to measure local temperature fluctuations. They conducted measurements along the entire boiling curve with water. The measured fluctuation amplitude was observed to increase with increasing surface superheat between about 3 K in nucleate boiling and about 15 K close to the Leidenfrost point. Nishikawa et al. reported also different signal characteristics for different boiling regimes. Lee et al. (1985) carried out transient quenching experiments with water and measured local temperature fluctuations with a miniature thermocouple. Referring to their results, typical temperature drops during rewetting of the surface were as large as 125 K. More recently, Shoji et al. (1991) also measured local temperature fluctuations using a miniature thermocouple. They used also water as test fluid. The measured temperature fluctuations also increased with increasing heater superheat. The observed fluctuation amplitude was between about 15 K in nucleate boiling and about 50 K in transition boiling close to the Leidenfrost point. Hohl et al. (2000) measured with an array of MTCs local temperature fluctuations with FC-72 as test liquid. Their results agree also with the current results with respect to general characteristics. However, a detailed comparison of the results is difficult. First, the properties of the employed liquids are highly different to those of isopropanol used here. For example, Δh_{lv} of water is about 3.4 times larger than Δh_{lv} for isopropanol; Δh_{lv} of FC-72 is just about 10% to that of isopropanol. Second, the physical dimensions of the thermocouples are different and therefore the amount of area monitored. This holds especially for the distance between the surface and the junction. Third, the local thermal properties of the thermocouples used for some of the studies are very different to the MTCs used here, for example thermal conductivity. This has an effect on the measured amplitude. Forth, the conditions for signal conditioning and/or signal acquisition are often not fully specified. Signal bandwidth (and proper setting of sampling rate, at least twice the cutoff frequency) can affect the signals to a large amount as can be seen in Fig. 13. The figure depicts the measured signal and three additional curves, which show the simulated effect of a reduced bandwidth during acquisition. The additional curves are calculated using the same signal, but a digital zero-phase lag (for easier comparison) lowpass filter order 4 with the cutoff frequency as given in Fig. 13. The reduced slope of the temperature curve leads to a large underestimation of the instantaneous surface heat flux at the temperature drop, for example.

Selected frames of the measured temperature field are depicted in Fig. 14 for nucleate boiling at a superheat 0.5 K below CHF. These frames represent a short sequence of 18.4 ms. Red color represents high superheat, blue color low superheat. At 0 ms, no hot spots can be seen—most of the measured area has a low temperature pointing to ongoing nucleation and vapor generation. In the next subsequential frames, the temperature at the

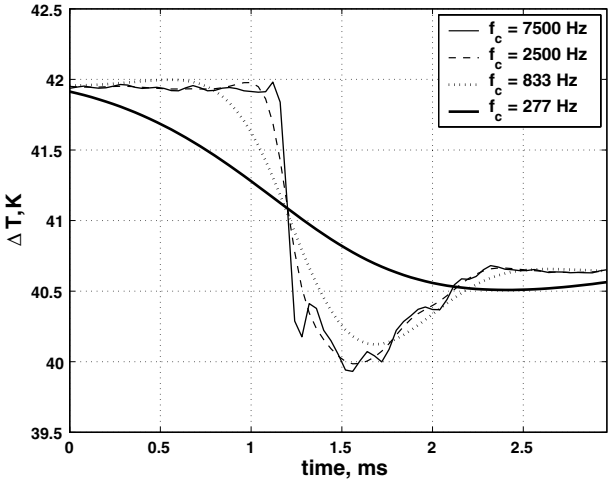

Fig. 13. Effect of acquisition bandwidth on signal characteristics during a temperature drop.

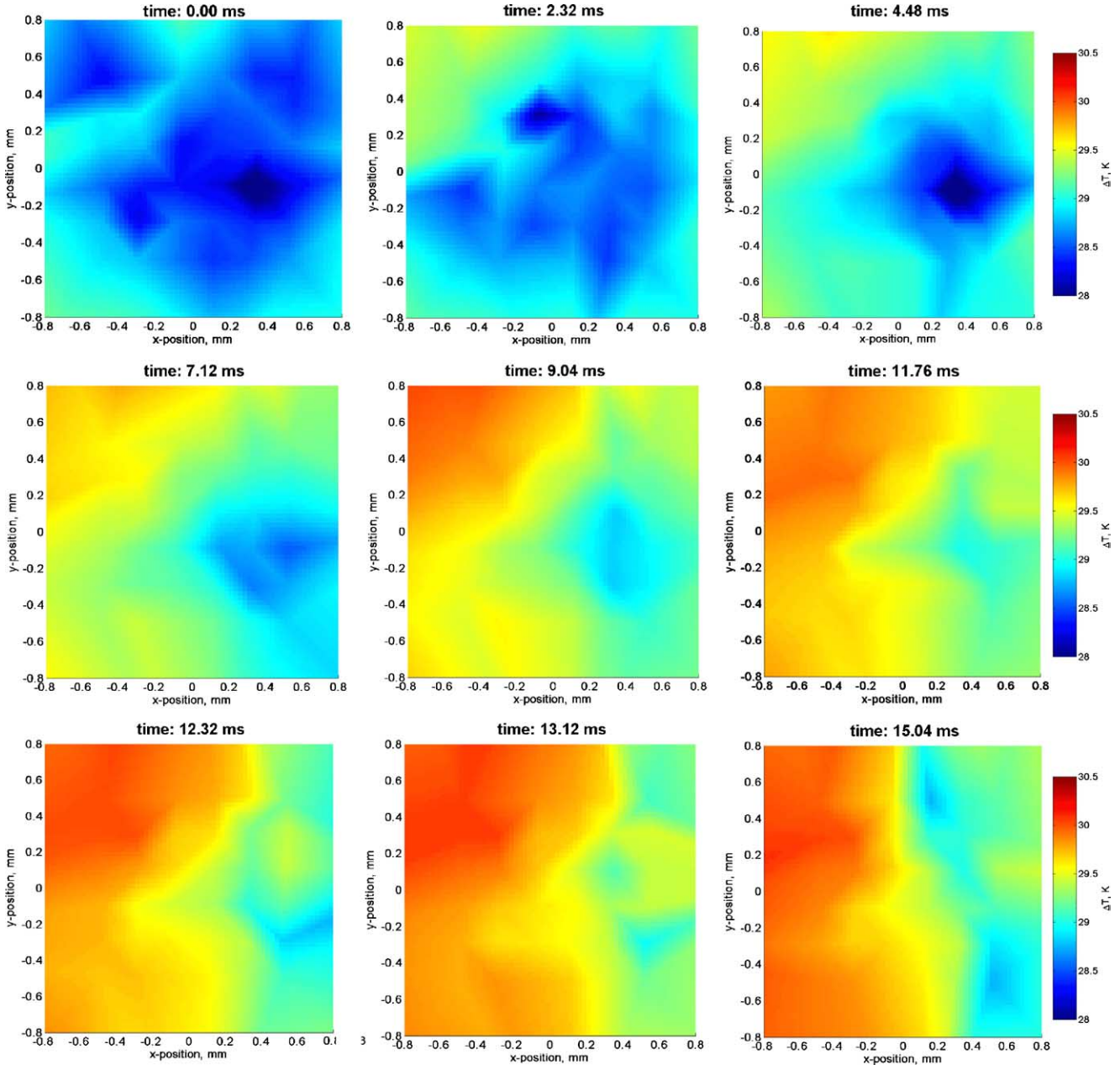

Fig. 14. Selected local temperature fields in nucleate boiling close to CHF. X and Y positions see Fig. 7. A color version of this figure can be found on http://www.sciencedirect.com which enables a better display of the important features.

upper left corner starts to increase. At 11.76 ms, about 50% of the MTCs representing the half measured area indicate high temperature. At $t = 15.04$ ms—and the next four frames—a steep temperature gradient can be seen across a borderline located approximately from bottom to top. While the temperature on the left hand side remains more or less similar, the temperature field on the right hand side contains few local temperature minima. During the next frames, the locations of the temperature minima change, but the location of the main borderline moves comparatively slow to the lower left corner. At the end of the sequence, the hot zone cannot be seen anymore. The measured temperature fields are most likely caused by a temporarily existing dry spot, which moves across the surface and covers a fraction of the MTC field during this process. The similar temperature within the high temperature zone points to a uniform—and low—heat transfer in this area, which can possibly be explained only by the existence of a temporarily existing vapor film at the surface at such high superheat. Otherwise, some temperature drops caused by nucleation of bubbles would be detected within this zone in the sequence. Nucleation/rewetting of the surface can be seen within the other half

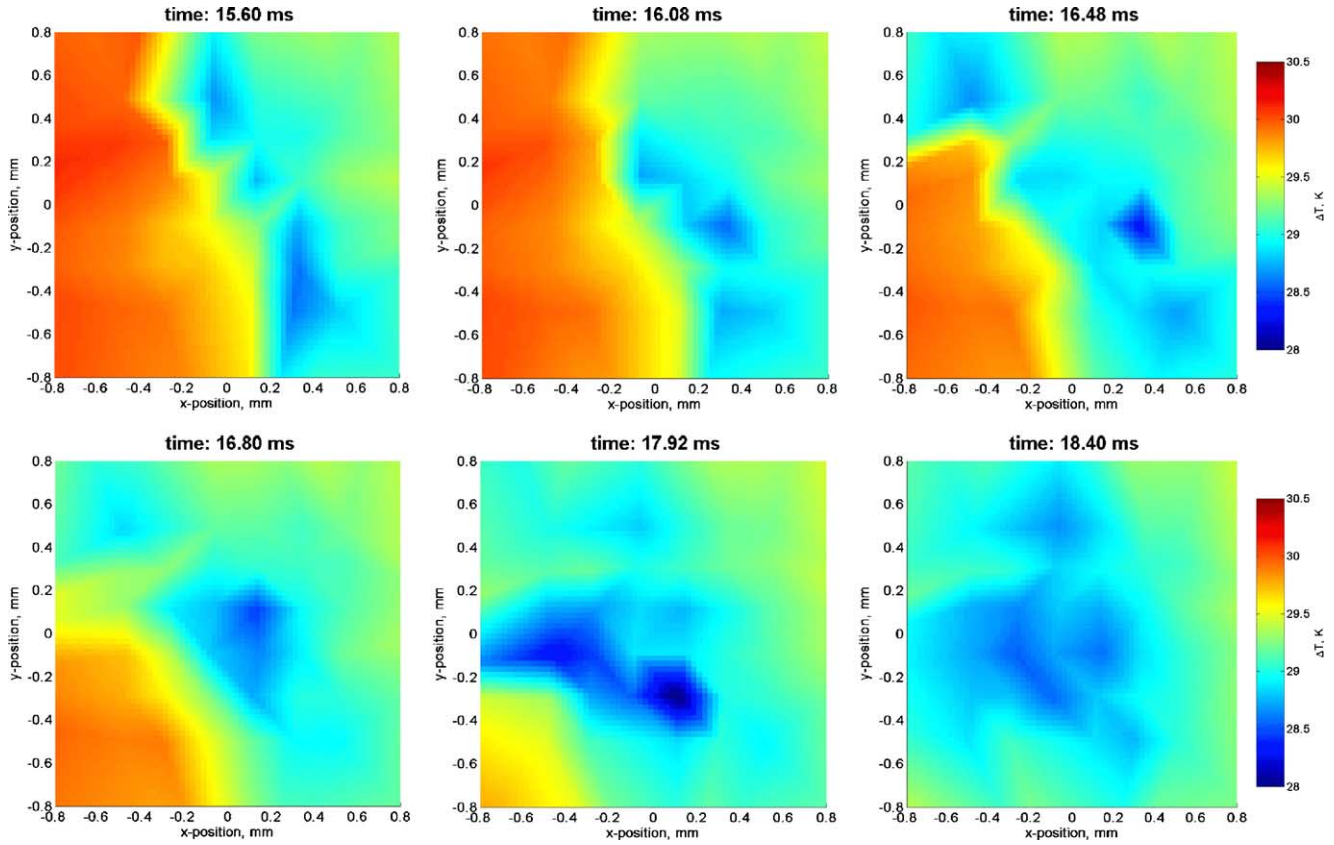

Fig. 14 (*continued*)

of the field. Here, the "switching" locations of temperature minima point to nucleation and surface rewetting. Therefore the existence of dry spots in nucleate boiling close to CHF on thick heaters can be confirmed.

5.2. Optical probe experiments

5.2.1. Phase indicator function

PIF traces of all four optical probes for a distance between lower probe and the heater surface of 20 mm are depicted in Fig. 15 for nucleate boiling and CHF and in Fig. 16 for transition and film boiling. The same boiling set-points but for a probe distance of 8 μm is plotted in Figs. 17 and 18. High signal level represents vapor, low level liquid phase at the probe tip. For these plots, the PIFs of probes two, three and four are level shifted to enable better comparison.

Although a true representation of the signal with a few plots is difficult, the PIF traces give some information on the typical characteristics of liquid–vapor fluctuations in the different boiling regimes. The representation in a few plots is difficult because liquid–vapor changes occur on very different time scales. As can be expected, these time scales are changing with a change of the boiling regime. But even more complicated, the liquid–vapor fluctuations for a given boiling setpoint do occur on very short time scales and also on much longer time scales. A good example for this property can be found in the bottom plot of Fig. 15 (CHF). Thus,

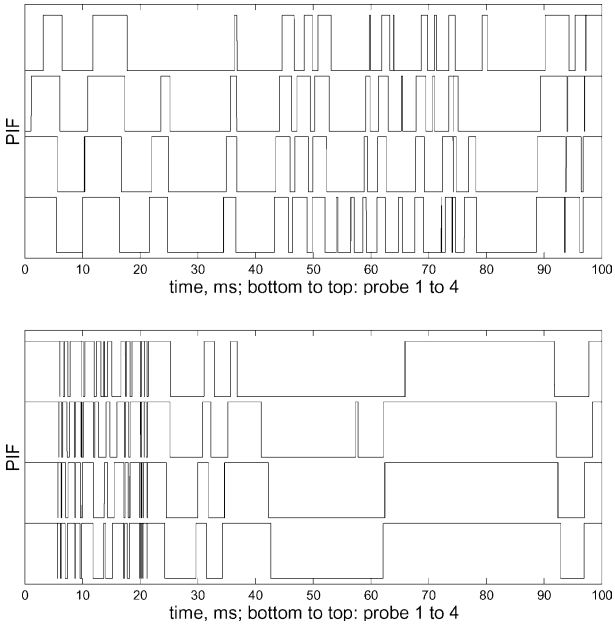

Fig. 15. PIFs at 20 mm probe distance, top: nucleate boiling ($\dot{q} = 14.2$ W/cm^2), bottom: CHF.

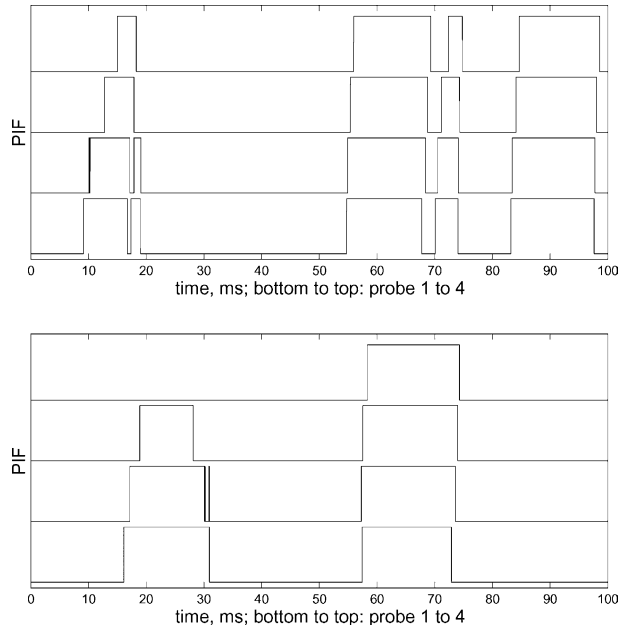

Fig. 16. PIFs at 20 mm probe distance, top: transition boiling ($\dot{q} = 10$ W/cm^2), bottom: film boiling ($\dot{q} = 5.5$ W/cm^2).

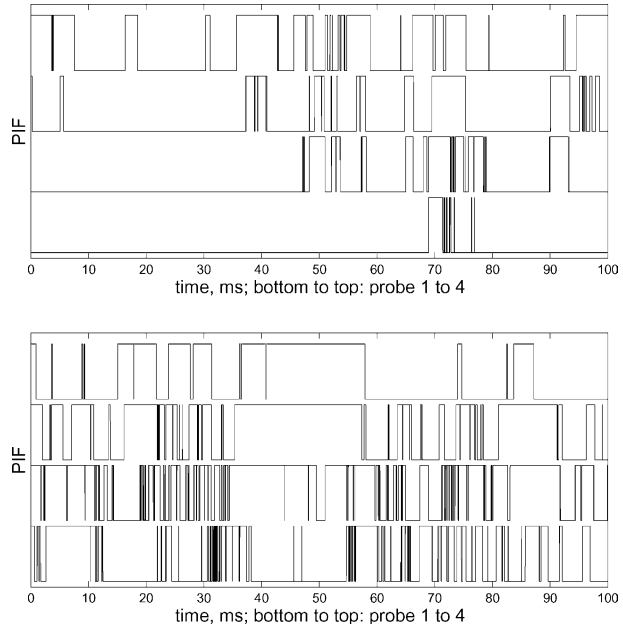

Fig. 17. PIFs at 8 μm probe distance, top: nucleate boiling ($\dot{q} = 14.2$ W/cm^2), bottom: CHF.

calculation of mean values of any kind with good confidence requires analysis of much longer PIF sections than plotted in Figs. 15–18.

Besides the difficulties regarding the selection of a short "representative" PIF section, some typical characteristics of liquid–vapor fluctuations can be found in the plotted PIFs. At 20 mm probe distance (Figs. 15 and 16), the signals at all four probes appear very similar.

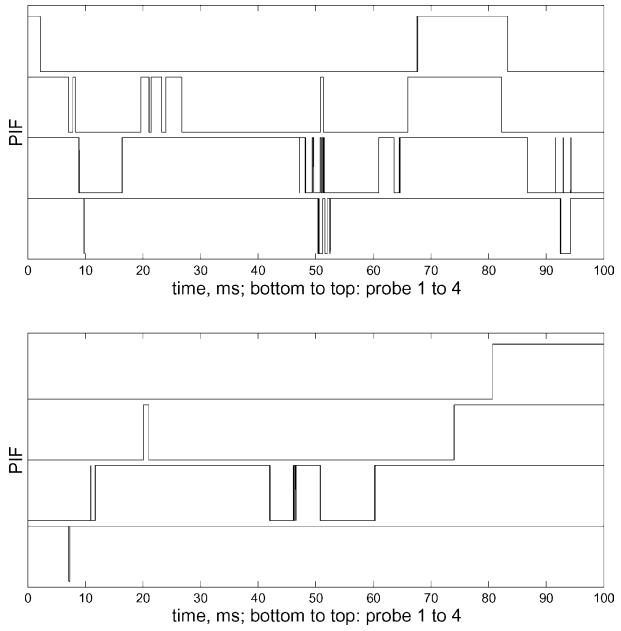

Fig. 18. PIFs at 8 μm probe distance, top: transition boiling ($\dot{q} = 10$ W/cm^2), bottom: film boiling ($\dot{q} = 5.5$ W/cm^2).

This leads to some conclusions. First, the flow does pass the 4-tip probe without a relevant effect on the flow properties occurring at this probe position. If the latter would be the case, the signal should be altered from one probe to the next probe. "Missing bubbles", as the missing vapor peak at probe 4 in the bottom plot in Fig. 16 for example are expected to occur from time to time because of different radial probe positions and flow components in X- and Y-directions. Second, the direction of the flow is facing upwards, as can be expected. Otherwise, much more "missing bubbles" and less correlated signals should be found. Third, the flow is more or less established because of similar properties at all probes. The cross correlations (see later in this section) point also towards this interpretation.

Large differences of the two phase flow characteristics in the different boiling regimes at 20 mm probe distance can be seen in the plots. In nucleate boiling up to CHF, many vapor contacts are found. With increasing heat flux, an increased number of longer vapor contacts are detected. These longer contacts are expected due to bubble coalescence. Very rapid fluctuations caused by small bubbles are also found. In low heat flux transition and film boiling, few but relatively long vapor contacts are detected. This behavior is caused by large bubbles leaving the stable vapor film in film boiling or from the partially and temporarily dry patches in transition boiling. Therefore more and also shorter contacts are found in transition boiling than in film boiling. This behavior is also well known from video or photographic observations. In transition boiling, the MTC signals (see

Fig. 12, top) point also to surface wetting and subsequent nucleation and therefore generation of bubbles.

The flow characteristics change considerably at the closest measured probe distance. Generally, the PIF characteristics are very different at all probes for a given boiling setpoint within the heater nearfield. Because of this behavior, the probes are expected to be located in zones of different flow characteristics. In nucleate boiling and CHF (see Fig. 15), the void fraction at the lowest probe is much less than for the probes above. The mean duration and number of vapor contacts differs also considerably between the probes. In transition and film boiling, the situation is different. Here, the void fraction is highest at the lowest probe and decreases with increasing probe distance. This is not surprising because a stable or unstable vapor film is expected in film and low heat flux transition boiling, respectively. For the measurements very close to the heater surface, a more advanced analysis is expected to uncover typical flow characteristics, see also later in this chapter the paragraphs on cross correlation coefficients.

5.2.2. Void fraction

The mean void fraction at the lowest probe for all measured probe positions and various wall superheats are plotted in Fig. 19. Fig. 20 gives a zoom into the plots of Fig. 19 for the heater nearfield region.

The void fraction at the closest measured distance to the heater (8 μm) increases monotonically from low surface superheat towards CHF. For all measurement points between nucleate boiling CHF, a liquid rich layer directly at the heater surface is found. A distinctive local maximum of the void fraction can be seen for all points between moderate boiling heat flux and CHF. The distance at this maximum moves towards smaller heater distances for increasing surface superheat or heat flux. If we assume the distance at this peak of the void fraction curve as a measure of the thickness of the liquid-rich zone, its thickness decreases monotonically with increasing superheat. Using the definition above, the thickness changes from 850 μm at $\dot{q} = 23.9$ W/cm^2 down to 100 μm at CHF. This trend can be also seen in high heat flux transition boiling.

The situation is different in low heat flux transition boiling and film boiling (see lowest plots in Figs. 19 and 20, respectively). In these regions, no drop of the local void fraction close to the heater surface can be seen. Here, the maximum of the void fraction is located at the smallest measured distance.

The void fraction curves show also a local minimum for boiling setpoints between medium heat flux nucleate boiling and film boiling. Position and value of this minimum are more or less independent of heat flux between medium heat flux nucleate boiling and CHF. Here, the minimum of about $\alpha_v \approx 0.3$ is located at about 4.5 mm distance. The void fraction at the greatest

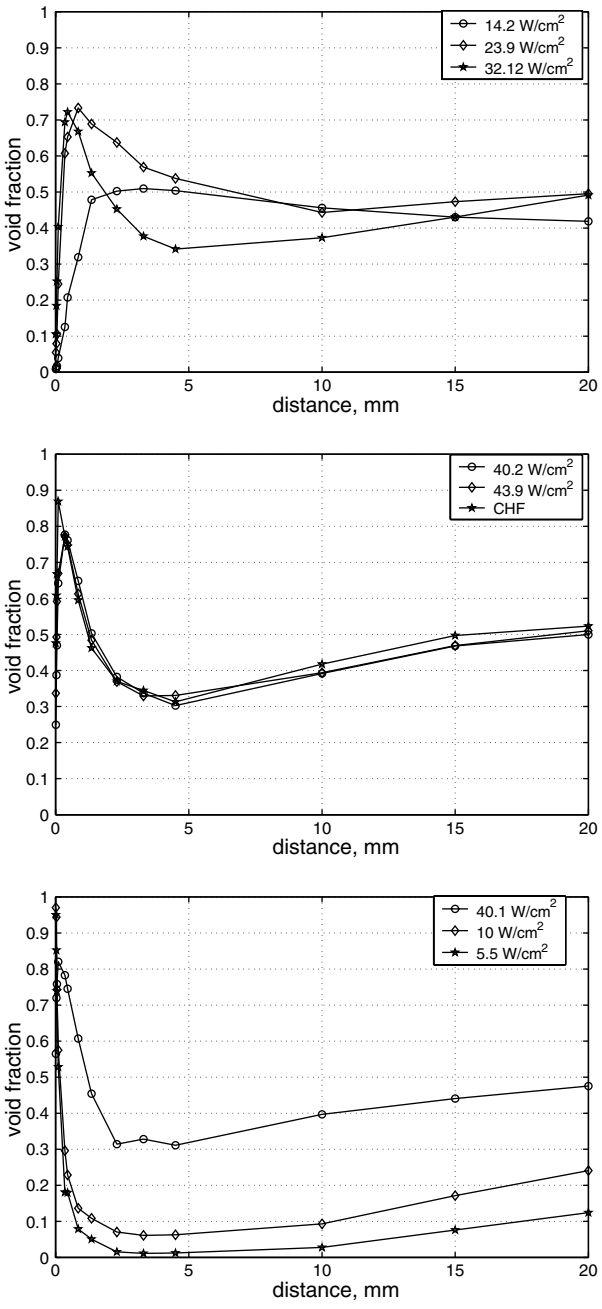

Fig. 19. Mean void fraction for entire distance range, top: nucleate boiling, middle: nucleate boiling up to CHF, bottom: transition and film boiling.

measured distance (20 mm) is also more or less constant in nucleate boiling up to CHF with $\alpha_v \approx 0.5$. These surprising findings are discussed in the paragraphs on cross correlation later in this chapter.

Void fraction data has not been calculated yet for probes nos. 2, 3 and 4 due to the large computation time (see Section 4.4). Calculation of α_v requires analysis and therefore calculation of the entire PIF section. So far, only short PIF sections for these probes at selected probe positions have been calculated in order to plot the

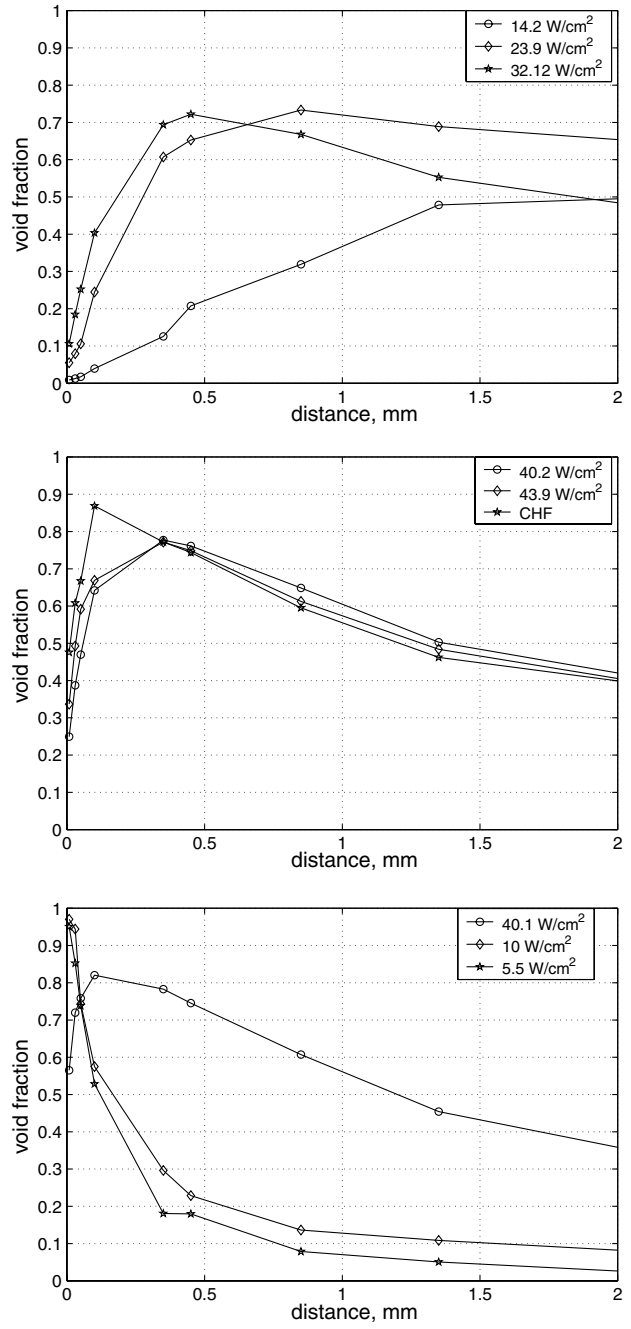

Fig. 20. Mean void fraction for 8 μm to 2 mm distance, top: nucleate boiling, middle: nucleate boiling up to CHF, bottom: transition and film boiling.

PIFs (see Figs. 15–18) and the correlations (see next paragraph).

Some results on mean void fraction above a horizontal heater at saturated conditions are given in the literature. Unfortunately, the results are mostly measured with water as test fluid boiling at atmospheric pressure, for example Iida and Kobayasi (1970) and Shoji (1992) with the exception of Bonetto et al. (1993) and Hohl et al. (1998) who used FC-72. The results of Iida and Kobayasi and Shoji et al. agree to the presented data in general. They report a liquid rich zone close to the heater in nucleate boiling and a high void zone next to the surface in transition boiling. They also report the same general trends with the exception of the results of Shoji et al. for large distances to the heater: here, the void fraction converges to zero. Also for the results measured with FC-72, the general trends are identical despite some data scatter for the heater near field in the results of Bonetto. The results of Hohl et al. for all boiling regions are very close to the current results in terms of void fraction curve shapes, but for different distances to the heater surface. However, a detailed comparison of the results is difficult because of the different fluids used for the studies in the literature. To the authors knowledge, no void fraction data on isopropanol or other alcohols is currently available in the literature with the exception of a single boiling setpoint measured with a predecessor of the current heater by Lüttich et al. (2001). The latter data also agrees with the current results.

5.2.3. Cross correlation

Short sections containing the peak of the cross correlation coefficient of probe combinations 1–2, 2–3 as well as 3–4 are plotted in Fig. 21 for 4.5 and 20 mm distance between heater surface and lowest probe in nucleate boiling up to CHF. For all plots of Fig. 21, the curves with large peak values are correlations of the 4-tip optical probe located at 20 mm distance, the second set of curves represent measurements at 4.5 mm distance. The peak location is used to calculate the time difference for a calculation of a mean velocity. As can be seen, the peak values decreases monotonically with increasing probe-to-probe distance (see Table 1). It decreases also with decreasing distance between the correlated probes and the heater surface. The latter can be interpreted as an indicator for a changing flow regime at these positions. Ongoing coalescence of bubbles and higher turbulence than at the upper position could be an explanation for the decreased peak value at 4.5 mm probe position because both effects would cause a higher number of independent events at compared probes and thus a decreased correlation peak maximum. The decrease of the maximum peak value with increasing distance between the compared probes is somewhat surprising. A small axial probe distance is expected to cause an increased relative timing jitter at correlated events because of bubble interface curvature as the radial probe distance for all probe combinations remains constant ($\Delta s = 125$ μm). At the lowest two probes the relation between radial and axial probe distance is 125/160 μm, at the uppermost probes three and four 125/330 μm. Assuming bubbles with constant rise velocity and direction, the signals at a larger distance between the correlated probes are expected to be better correlated as

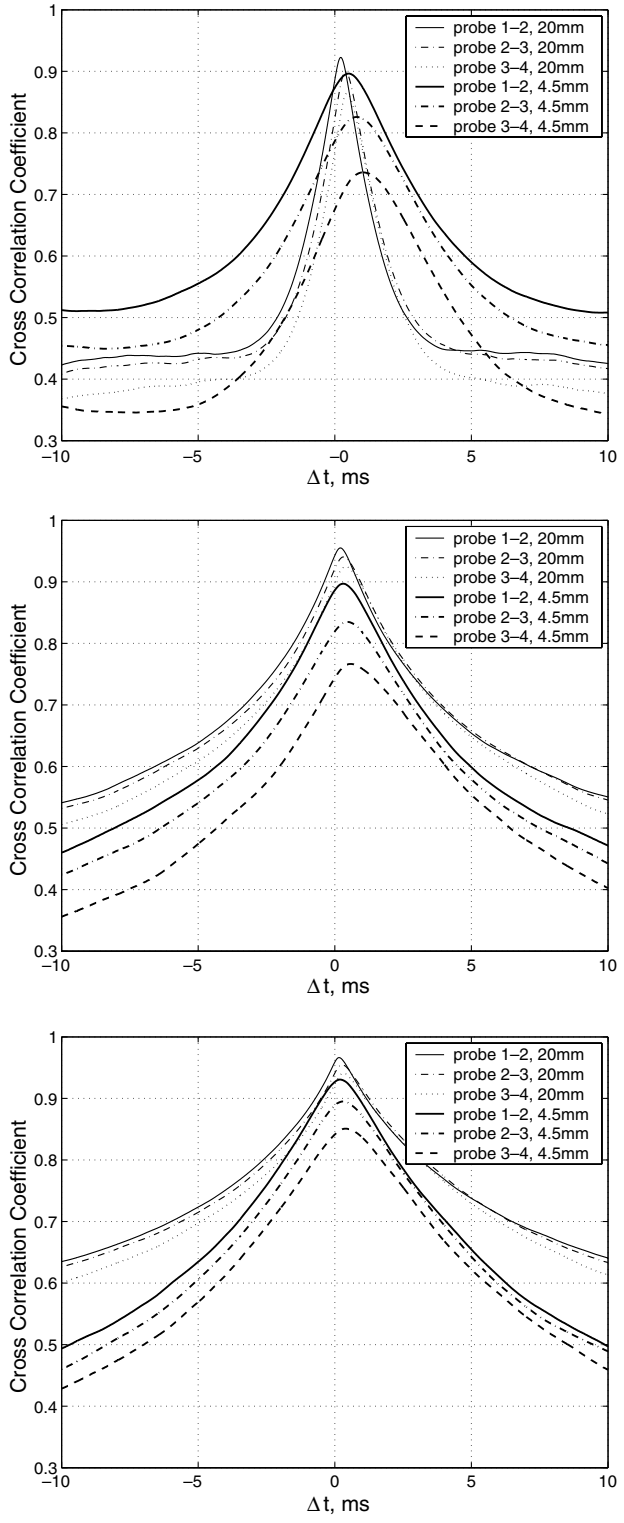

Fig. 21. Cross correlation coefficients for 20 and 4.5 mm probe distance of probe 1, nucleate boiling (top) to CHF (bottom).

the passage time because of rise velocity becomes more dominant over time differences caused by different interface detection locations at both probes resulting from bubble curvature. As can be seen in the plots of Fig. 21, the trend is opposed to this expectation. This effect will be investigated in the future.

Table 3
Mean velocity at 4.5 and 20 mm probe positions for nucleate boiling up to CHF

	Probe 1–2	Probe 2–3	Probe 3–4
Distance between heater surface and lowest probe: 4.5 mm			
$\dot{q} = 14.2$ W/cm^2	0.31 m/s	0.32 m/s	0.32 m/s
$\dot{q} = 32.1$ W/cm^2	0.53 m/s	0.58 m/s	0.56 m/s
CHF	0.82 m/s	0.81 m/s	0.81 m/s
Distance between heater surface and lowest probe: 20 mm			
$\dot{q} = 14.2$ W/cm^2	0.73 m/s	0.66 m/s	0.73 m/s
$\dot{q} = 32.1$ W/cm^2	0.78 m/s	0.8 m/s	0.82 m/s
CHF	1 m/s	0.98 m/s	1.05 m/s

The time differences at the peak maxima are also different for the three probe combinations. These differences are mostly caused be different distances between the correlated probes, see Table 1. The calculated mean velocities using Eq. (3) for the probe combinations 1–2, 2–3 as well as 3–4 are listed in Table 3 for 4.5 mm (top) and 20 mm probe position (bottom).

Disregarding the minor effects described above, the calculated velocities are helpful for an interpretation of the void fraction profiles of Figs. 19 and 20 (see Section 5.2.4). This holds even more as the calculated velocity values at different probe combinations—at approx. constant probe position—are very similar.

5.2.4. Interpretation of the optical probe results

The void fraction values at 20 mm distance—and to a minor extent also at 4.5 mm—are almost independent of heat flux between fully developed nucleate boiling and CHF (see Figs. 19 and 20). This finding is not expected because the vapor mass flux is expected to increase with an increase of heat flux at a given location and so should also increase α_v. Moreover, the void fraction at 20 mm distance is always higher than at the lower probe location. Four possible technical reasons can cause a change of the detected void fraction with a change of distance and/or heat flux. First, a change of flow (vapor) velocity, second re-evaporation of fluid, third contraction of the global vapor flow above the heater and also measurement error. Measurement error is unlikely because all four probes detect similar values. Re-evaporation of the fluid can be a possible cause for an increase of void fraction with increasing distance, but here the change of void fraction seems much too large to be mainly caused by re-evaporation at the relatively large (4.5 and 20 mm) distances. Re-evaporation is not expected to be relevant for a change of void fraction at constant probe location but a change of heat flux for the boiling range under consideration. A change of velocity can be a cause for both findings. A velocity increase with increasing distance would result in a decrease of void fraction. Exactly the opposite is found:

both void fraction and velocity increase at the larger distance. Thus, only contraction of the global two-phase flow can cause the increase of void fraction at large heater distances. Contraction of the global flow would cause the probe to measure vapor representing a larger heater area. This effect will be investigated in the future using a high speed video camera. For a constant probe position, the finding for α_v can be explained by the mean velocity because the velocity increases with increasing heat flux which allows a larger vapor mass flux to be transferred at constant α_v. Contraction of the global two-phase flow is expected to play a minor role at a constant probe position.

An analogous reasoning holds for the steep decrease of the void fraction profiles between the local void fraction maximum (between nucleate boiling and CHF) and the local minimum at about 4.5 mm distance. Here, an acceleration of the vapor structures can explain the decrease of the void fraction. At this small distance, re-evaporation can possibly play a relevant role, but re-evaporation would result in an *increase* of void fraction which is opposed to the measured profiles. The void fraction profiles as well as an estimation of velocities at close distances will be the object of future investigations.

The steep increase of void fraction directly above the heater surface in nucleate boiling up to CHF can be explained as follows. Assuming a truly spherical shape of the bubbles during their growth period at the heater surface, the void fraction *directly* at the heater surface should approach *zero* independently of heat flux because of the bubble geometry. At larger distances—but less than the "average" bubble diameter—the *average* void fraction increases also because of geometry reasons. This effect can be illustrated as follows: assuming a layer of bubbles on the surface with any spacing in between the sites, the calculation of the average void fraction for a plane parallel to the surface at a distance z results in a similar shape of the average void fraction as detected by the probes (see Fig. 20). Therefore the location of the void fraction peak is possibly closely linked with the average bubble diameter. As can be seen in Fig. 20, the void fraction in nucleate boiling at 8 μm distance does not exactly approach zero—it decreases with decreasing distance. But the value at this distance increases with the commonly observed increase of nucleation site density associated with a increase of heat flux. This leads to the expected conclusion that the lower half of the bubble shape is not exactly spherical as proved by many bubble observation studies. A larger contact area between surface and bubbles as with truly spherical bubbles leads to a void fraction at the surface approaching a low, but nonzero value as detected by the probes. The extension of the reasoning in this paragraph to distances greater than the peak maximum is however more complicated as bubbles start to detach and move upwards. To make the situation even more complex, detached bubbles are much more subjected to and influenced by fluid motion induced by nucleating bubbles nearby than bubbles still sticking on the surface. A more detailed analysis will be focused on this problem in the future.

6. Conclusion

Special Microthermocouples (MTCs, 38 μm diameter) for measurements of temperature fluctuations 3.6 μm below the heater surface have been developed. Thirty-six MTCs are arranged on an area of 1 mm^2 with additional eight MTCs surrounding this field. A 4-tip optical probe for measurements of two-phase flow characteristics has also been developed. A tip size below 1.5 μm enables measurements very close to the surface with a minimum of flow disturbance.

Steady-state measurements with MTCs and the 4-tip optical probe are realized along the entire boiling curve using a temperature controlled heater (7 mm thick, diameter 35 mm) with saturated isopropanol at 0.104 MPa pressure.

MTC measurements enable analysis of surface wetting and bubble nucleation characteristics. In transition boiling, very short temperature transients exceeding −10 000 K/s can be found. Visualization of the temperature field proves the existence of dry patches on the surface *before* CHF is reached. No rapid temperature fluctuations and therefore surface wetting can be found in film boiling.

Optical probe measurements prove the existence of a liquid rich zone at the heater surface. This zone is found in nucleate boiling up to CHF and also in high heat flux transition boiling. Void fraction profiles are presented for measurements over a wide range of probe positions along the entire boiling curve. The shape of the void fraction curves can be explained with calculated mean velocities using cross correlation coefficients of the probe combinations.

Acknowledgements

The authors highly appreciate financial support the by Deutsche Forschungsgemeinschaft DFG in the frame of a joint research project on fundamentals of boiling heat transfer. The project was supported with bidirectional optical fiber units Bidi® by Infineon AG, Germany.

References

Arosio, S., Bertola, V., Fossa, M., 1999. Comparative analysis of intermittent air–water flow structure by means of different mea-

surement techniques. In: Proc. Two Phase Flow Modelling and Experimentation 3, 1359–1364.

Bonetto, F., Clausse, A., Converti, J., 1993. Two-phase flow in the localized boiling field adjacent to a heated wall. Int. J. Heat Mass Transfer 36, 1367–1372.

Buchholz, M., Auracher, H., 2002. Improved optical probes and their validation for local measurements in two phase flows. In: Proc. German–Japanese Workshop on Multiphase Flow, Forschungszentrum Karlsruhe, Germany, FZKA-6759, B1–B10.

Hohl, R., 1999. Mechanismen des Wärmeübergangs beim transienten und stationären Behältersieden im gesamten Bereich der Siedekenlinie. Ph.D. thesis, Technische Universität Berlin, VDI Fortschritt-Berichte Series 3, No. 597.

Hohl, R., Blum, J., Auracher, H., Marquardt, W., 1998. Characteristics of liquid–vapor fluctuations in pool boiling at small distances from the heater. In: 11th Int. Heat Transfer Conf., vol. 2. Kyongju, Korea.

Hohl, R., Blum, J., Buchholz, M., Lüttich, T., Auracher, H., Marquardt, W., 2000. Boiling experiments under steady state and controlled transient conditions. In: Proc. Boiling 2000: Phenomena & Emerging Applications, vol. 1. Anchorage, Alaska USA, pp. 236–252.

Iida, Y., Kobayasi, K., 1970. An experimental investigation on the mechanism of pool boiling phenomena by a probe method. In: Proc. 4th Int. Heat Transfer Conf., vol. 5 B1.3. Paris, France.

Kenning, D., Kono, T., Wienecke, M., 2001. Investigation of boiling heat transfer by liquid crystal thermography. Exp. Therm. Fluid Sci. 25, 219–229.

Kim, J., Benton, J., Wisniewski, D., 2002. Pool boiling heat transfer on small heaters: effect of gravity and subcooling. Int. J. Heat Mass Transfer 45, 3919–3932.

Lee, L., Chen, J., Nelson, R., 1985. Liquid–solid contact measurements using a surface thermocouple temperature probe in atmospheric pool boiling water. Int. J. Heat Mass Transfer 28, 1415–1423.

Luke, A., 2003. Thermo and fluid dynamics in boiling, connection between surface roughness, bubble formation and heat transfer. In: Proc. 5th Int. Boiling Heat Transfer Conf., Montego Bay, Jamaica, 4–8 May.

Lüttich, T., Buchholz, M., Hertel, C., Marquardt, W., Auracher, H., 2001. Pool boiling at high heat fluxes (part II): modeling and identification of two phase flow characteristics close to the heater surface. In: Proc. Int. Refrig. Conf. Comm. B1, Paderborn, on CD-ROM.

Lüttich, T., Buchholz, M., Marquardt, W., Auracher, H., 2003. Towards a unifying heat transfer correlation for the entire boiling curve. In: Proc. 5th Int. Boiling Heat Transfer Conf., Montego Bay, Jamaica, 4–8 May; submitted to Int. J. Therm. Sci.

Moore, F., Mesler, R., 1961. The measurement of rapid surface temperature fluctuations during nucleate boiling of water. AIChE J. 7, 620–624.

Nishikawa, B., Fuji, T., Honda, H., 1972. Experimental study on the mechanism of transition boiling heat transfer. Bull. JSME 15, 93–103.

Nishio, S., Gotoh, T., Nagai, N., 1998. Observation of boiling structures in high heat flux boiling. Int. J. Heat Mass Transfer 41, 3191–3201.

Sadasivan, P., Unal, C., Nelson, R., 1995. Perspective: Issues in CHF modeling—the need for new experiments. ASME J. Heat Transfer 117, 558–567.

Shoji, M., 1992. A study of steady transition boiling of water: experimental verification of macrolayer evaporation model. In: Proc. Engng. Found. Conf. Pool and External Flow Boiling. Santa Barbara, USA, pp. 237–242.

Shoji, M., Witte, L., Yokoya, S., Kawakami, M., Kuroki, H., 1991. Measurement of liquid–solid contact using micro-thermocouples in pool transition boiling of water on a horizontal copper surface. In: ASME/JSME Thermal Engng. Proc., vol. 2, pp. 333–338.